JOURNAL OF PROPULSION AND POWER
Vol. 25, No. 6, November–December 2009

Hardware-in-the-Loop Testing of a Fuel Cell Aircraft Powerplant

Thomas H. Bradley*
Colorado State University, Fort Collins, Colorado 80523
Blake A. Moffitt, Dimitri N. Mavris, and Thomas F. Fuller
Georgia Institute of Technology, Atlanta, Georgia 30332
and
David E. Parekh
United Technologies Research Center, East Hartford, Connecticut 06108

DOI: 10.2514/1.40805

This paper presents the experimental methods and test results of a hardware-in-the-loop simulation of the powerplant for a small-scale fuel-cell-powered unmanned aerial vehicle. In this study, the hardware associated with the powerplant, power train, energy storage, and control systems operates dynamically as a component within a real-time aircraft simulation routine. Control signals, electrical loads, and mechanical loads are applied to the hardware to emulate the conditions of operation of the unmanned aerial vehicle powerplant during flight. Experimental results from hardware-in-the-loop testing of the fuel cell power train are presented with uncertainty analysis and discussion. These results show new aspects of the performance of fuel cell unmanned aerial vehicle powerplants, including the powerplant performance during long-endurance missions, power train subsystem power consumption, and unmodeled fuel cell dynamics. A comparison of the measured powerplant performance to experimental results from the literature shows that the fuel cell powerplant can outperform advanced electrochemical energy storage and internal combustion powerplants at the scale of the hardware-in-the-loop aircraft.

Nomenclature

C_D	=	aircraft coefficient of drag
C_L	=	aircraft coefficient of lift
C_q	=	propeller coefficient of torque
C_{rr}	=	coefficient of rolling resistance
C_T	=	propeller coefficient of thrust
D	=	drag force, N
d	=	propeller diameter, m
E	=	propulsive energy, J
E^{O}	=	standard potential of the oxygen reduction reaction, 1.229 V
g	=	acceleration due to gravity, m/s^2
h	=	aircraft altitude, m
h_{desired}	=	desired aircraft altitude, m
h_{error}	=	error in aircraft altitude, m
I_{sp}	=	specific impulse, s
J	=	propeller advance ratio
L	=	lift force, N
m	=	aircraft mass, kg
m_{power}	=	powerplant mass (including power train, fuel, and tankage), kg
n_{cells}	=	number of cells in the fuel cell stack
P_{H2}	=	hydrogen pressure in the fuel cell anode manifold, Pa
Q	=	propeller and electric motor torque signals, N · m
q_{H2}	=	flow rate of hydrogen, kg/s
S_w	=	wing area, m^2
s	=	range, m
T	=	thrust force, N
t	=	endurance, h
t_{cmd}	=	throttle command
t_{PWM}	=	pulse-width-modulated throttle command
v	=	airspeed, m/s
v_{desired}	=	desired aircraft velocity, m/s
v_{error}	=	error in aircraft velocity, m/s
W	=	weight force, N
α	=	angle of attack, rad
γ	=	climb path angle, rad
θ_{fc}	=	fuel cell temperature, °C
ρ	=	air density, kg/m^3
ϕ	=	bank angle, rad
ω	=	propeller rotational speed, rad/s
ω_{fans}	=	fuel cell stack fan rotational speed, rad/s

Received 4 September 2008; revision received 26 June 2009; accepted for publication 26 June 2009.

*Department of Mechanical Engineering, Engineering A103R; thomas.bradley@colostate.edu.

I. Introduction

SMALL-SCALE, electrically powered, unmanned aerial vehicles (UAVs) are currently in use performing a variety of reconnaissance and remote sensing missions. For these missions, electrically powered UAVs are generally preferred to small-scale internal combustion UAVs because of their low cost, reliability in the field, physical robustness, and simple rechargability. A desire for longer endurance than is available from the current generation of commercially available batteries has motivated the development of electrical UAV powerplants with higher specific energy [1,2]. These proposed powerplants incorporate fuel cells [3,4], advanced electrochemical energy storage [5], and hybrid electric systems [6,7]. These advanced powerplant designs often include dynamic subsystems, active controls, and other implementation challenges that will require new development methods and tools.

This paper presents a study of the performance of a fuel-cell-powered UAV using a hardware-in-the-loop (HIL) simulation of the aircraft in flight. HIL simulation is a paradigm of system synthesis, evaluation, and testing; wherein, a dynamic system can be emulated by immersing physical components of some of its subsystems within a closed-loop virtual simulation of the remaining subsystems [8]. HIL testing is currently used for aviation and automotive control system software development [8,9]. For the UAV powerplant application, HIL substitutes portions of the aircraft hardware with

software that can emulate the communication, loads, and kinematics of the aircraft systems. Interface components between the hardware and software allow for bidirectional information flow among the physical and virtual systems. HIL simulation of a fuel-cell-powered UAV enables this study to address some of the current research challenges associated with the design and development of fuel cell powerplants for UAVs.

For instance, a primary challenge to the development of fuel-cell-powered UAVs is measurement of the powerplant performance under flight conditions. To date, validation and performance testing of UAV powerplants has been primarily performed through flight testing. For example, Kosmatka [10], Bateman et al. [11], Tigner et al. [12], and Bradley et al. [13] have used test flights to validate powerplant and airframe design for prototype UAVs. Howard et al. [14] performed powerplant testing using a half-scale model. Compared with these flight testing methods described in the UAV literature, HIL simulation can be a more effective tool for performance characterization of complex powerplant systems. Data acquisition systems that are not flightworthy because of weight or size can be used during HIL for calibration and validation of system performance. Test conditions can be rigorously controlled, and the experimental uncertainty associated with HIL testing can be much lower than for flight testing. In all, HIL enables a more detailed measurement of the system behavior of the fuel cell powerplant and power train subsystem components.

Another challenge to the design of fuel-cell-powered UAVs is characterization of the dynamic performance of the fuel cell powerplant. In general, the fuel cell models used for design and development of fuel cell UAVs are static polarization curves based on isothermal, well-humidified, steady-state experimental data [15,16], as these are the data most often provided by manufacturers. Dynamic fuel cell polarization models (which can describe the effects of temperature, humidity, membrane water content, catalyst oxidation, and other relevant effects) are on the research frontiers of electrochemistry and are not suitable for system design [17,18]. Instead, the dynamics of the fuel cell system must be measured in situ. HIL allows for the repeatable experimental characterization of the effect of unmodeled fuel cell dynamics on flight performance.

Finally, studies disagree as to whether fuel cell powerplants are performance competitive with other UAV powerplant technologies, including batteries and internal combustion engines [3,19]. These comparisons are complicated by the novelty of the fuel cell UAV application and the lack of experimentally validated fuel cell UAV powerplant designs available in the literature. The HIL simulation performed for this study allows for the experimental measurement of the still-air endurance of a fuel-cell-powered aircraft. The performance of this powerplant can then be compared with more validity to experimental results for batteries and internal combustion engines from the literature.

This paper addresses these challenges through the development and testing of a HIL simulation of a fuel cell powerplant and aircraft. The aircraft and powerplant under test are the result of the fuel cell UAV design, development, and testing process documented in [3,13,15]. Section II presents the proposed architecture for the HIL simulation. The hardware, software, and interface components of the HIL simulator are described in Sec. III. Section IV presents experimental results with uncertainty analysis from the HIL testing of the fuel-cell-powered UAV power train completing a long-endurance mission. In Sec. V, discussion of the test results focuses on a breakdown of losses within the powerplant, a comparison of the HIL results to static models, and a performance comparison of various electrochemical and internal combustion powerplants. Section VI presents conclusions regarding the performance of the aircraft powerplant and the effectiveness of HIL testing in this application.

II. Hardware-in-the-Loop Simulation Architecture for Unmanned Aerial Vehicle Powerplants

Selection of a HIL simulation architecture consists of determining which components of the system under investigation will be represented in hardware and which will be represented in software, and defining the connections between them. The architecture selection must take into account the purpose and scope of the simulation.

In this study, HIL simulation is used to evaluate the range and endurance performance of a fuel cell UAV powerplant as it completes a simple mission. For a fuel cell UAV, the integrated powerplant and power train have been shown to be the primary source of aircraft performance uncertainty during design and development [15]. By using the actual powerplant and power train hardware during testing, the uncertainty associated with the performance simulation can be reduced. Conversely, the static performance of UAV airframes is well understood and can be accurately modeled by computer simulations [20]. Depending on the scalability and accuracy required of the computer simulation, the inputs to the software simulation can come from conceptual design algorithms, computational flow simulations, or experimental test results.

The proposed HIL simulation architecture is shown in Fig. 1. The simulation is composed of three categories of components: software simulation, hardware simulation, and interface. The software simulation contains the aircraft flight path, as well as the models of the autopilot, aircraft, and propeller. The hardware simulation contains all components of the energy storage system (powerplant, power train, and control system), excluding the propeller. The interface components actuate the hardware components and collect the inputs to the software simulation.

The arrows in Fig. 1 show the direction of the signal and energy flows between the components of the HIL simulation. The input to the HIL simulation is the desired aircraft flight path (h_{desired}, v_{desired}) in the form of an altitude and airspeed desired as a function of time. The error between the desired and actual flight path (h_{error}, v_{error}) is an input to the software autopilot simulation. The output of the autopilot simulation is a throttle command to the electric motor t_{cmd}. The signal generator interface translates the command from the software simulation to a transistor-to-transistor logic pulse-width-modulated (PWM) command t_{PWM} sent to the electric motor hardware. The electric motor is physically coupled to both the fuel cell stack via a dc electrical bus and to the dynamometer via a shaft coupling. The dynamometer provides the physical interface between the simulation hardware and software. The dynamometer applies a proportional-integral controlled torque to the electric motor based on the torque signal Q it acquires from the propeller simulation software. The inputs to the propeller simulation are the measured electric motor rotational speed ω and the simulated aircraft airspeed v. Based on these inputs, the propeller simulation calculates the propeller torque Q and thrust T. Propeller thrust is passed to the aircraft simulation that calculates the dynamic states of the aircraft. At the top of the diagram, the fuel cell hardware is outside of the aircraft dynamics

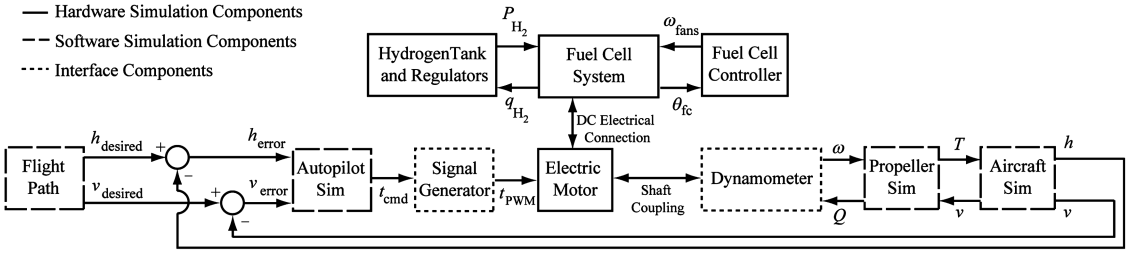

Fig. 1 Schematic and control system causality flowchart for HIL simulation.

loop. The fuel cell controller regulates the temperature of the fuel cell stack θ_{fc} by varying the fuel cell stack cooling fan speed ω_{fans}. The hydrogen tank regulators regulate the hydrogen pressure delivered to the fuel cell stack P_{H2}.

This HIL architecture allows for the efficient and accurate simulation of the powerplant performance of the fuel-cell-powered UAV by combining hardware and software models of the aircraft systems. The fuel cell and power train components are represented in hardware. These are the components that are novel and for which the detailed interactions are of research interest. The performance of these hardware components can be tested, controlled, tuned, and modified in hardware. The aircraft, propeller, and autopilot components are represented in software. These components are well-quantified technological commodities and are of lesser research interest in the context of aircraft flight performance prediction. The result is a HIL simulation that can model the system behavior of the entire aircraft in a more adaptable and repeatable testing environment.

III. Simulation Components

A. Simulation Hardware

The simulation hardware consists of the physical aircraft components, which are under experimental evaluation. For this study, this includes the hydrogen tank, regulators, fuel cell stack, fuel cell control system, and electric motor, as shown in Fig. 1. During the HIL tests, the fueling system and fuel cell powerplant are mounted to the laboratory bench top and are electrically connected to the other hardware.

The 300 W fuel cell stack (Horizon Fuel Cells H300) is the only source of electrical power for the aircraft components during testing. The stack is self-humidified and air cooled, and it requires only near-ambient cathode pressure. The stack is made up of 62 cells with $\sim$20 cm^2 of active area per cell. As shown in Fig. 1, the fuel cell control system controls the temperature of the stack θ_{fc} by dictating the speed of the cathode supply fans ω_{fans}. Increasing the cathode flow rate increases the evaporative cooling of the stack. This physical connection between the fuel cell air supply, water management, and cooling systems leads to a nonlinear and coupled relationship among cathode stoichiometry, membrane humidification, and stack temperature. To statically quantify the performance of the fuel cell stack before HIL testing, the stack current was measured at constant voltage for 400 samples at a sampling frequency of 4 Hz. Voltage steps were taken every 100 s with the fuel cell stack under its normal thermal and stoichiometric control. The resulting polarization curve for the fuel cell system is shown in Fig. 2, with a stack voltage model derived to fit the experimental data, using the methods of Kulikovsky [21]. The fuel cell stack temperature is controlled by the fuel cell control system as a function of stack current. The resulting stack temperature is stable at each test point but varies between 32°C at low current to 52°C at high current.

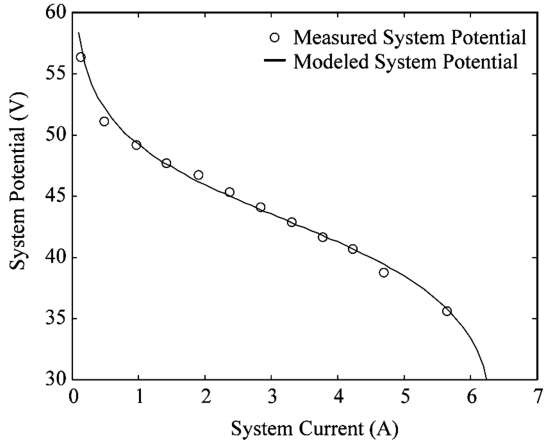

Fig. 2 Measured and modeled Horizon H300 fuel cell system polarization curve.

During HIL testing, ultrahigh purity hydrogen is supplied to the fuel cell using a laboratory hydrogen source. The hydrogen is delivered to the fuel cell anode at 34 kPa of gauge pressure. A periodic anode purge is controlled to maintain a hydrogen utilization of greater than 90%. The electrical power from the fuel cell powers the fuel cell control system hardware, the simulated aircraft flight controls (as simulated by a 12 V, 200 mA load), a simulated payload (as simulated by a 12 V, 120 mA load), and the propulsion electric motor (Neutronics 19102Y).

B. Interface Components

The interface components provide the physical and communication connections between the simulation software and the simulation hardware components. A custom signal generator is the communication connection between the autopilot simulation and the hardware of the fuel cell power train. The signal generator consists of a peripheral interface controller microcontroller that reads RS232 serial data from the autopilot simulation and outputs a PWM signal to drive the inputs of the electric motor controller. The commands to the signal generator are updated at 4 Hz.

The mechanical connection between the electric motor hardware and the propeller simulation software is made using a dynamometer developed for this application. A picture of the dynamometer is shown in Fig. 3. The electric motor is held in a bearing-suspended mount concentric to the motor rotational axis. Rotation of the motor mount is prevented by a strain gauged beam load cell that measures the torque output of the electric motor. The electric motor output shaft is coupled to the absorber and a tachometer via a flexible coupling. The absorber is a dc electrical generator for which the output is current-controlled by an electronic dc load (Hewlett–Packard 6050A). An analog tachometer measures the rotational speed of the electric motor shaft. The bandwidth of the dc load is greater than 1 kHz, potentially allowing a dynamic simulation of the aircraft at very high bandwidth. For this investigation, the dynamometer is controlled at a frequency of 4 Hz, appropriate for modeling of the aircraft climb/cruise dynamics and fuel consumption.

C. Simulation Software

The simulator software simulates the effects of the propeller, airframe, and flight controller on the power train hardware. The dynamic inputs to the propeller model are the airspeed of the aircraft v and the rotation speed of the electric motor shaft ω. The outputs of the propeller model are the thrust produced by the propeller and the torque applied to the electric motor [22]. The thrust T applied to the aircraft is defined by

$$T = \rho(\omega/2\pi)^2 d^4 C_T \tag{1}$$

The propeller torque Q to be applied to the electric motor is determined from the software propeller model using the relation

$$Q = \rho(\omega/2\pi)^2 d^5 C_q \tag{2}$$

Both the propeller thrust and torque coefficients C_q and C_T are functions of the aircraft airspeed, propeller rotational speed, and propeller diameter through the nondimensional propeller advance ratio:

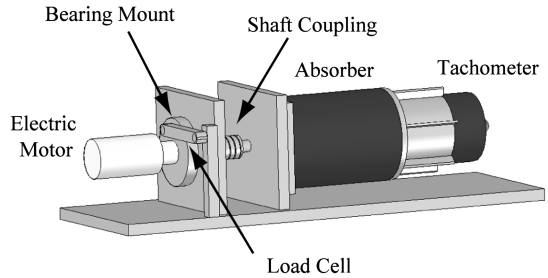

Fig. 3 Diagram showing the dynamometer configuration and components.

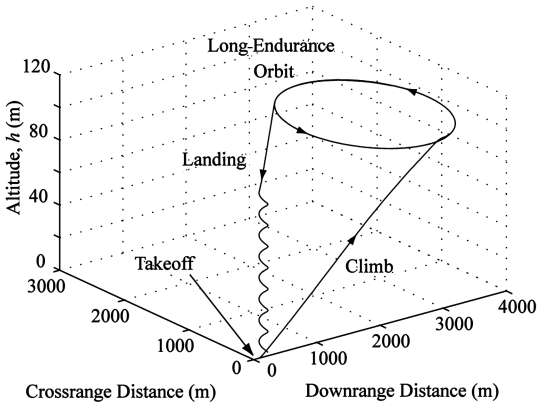

Fig. 4 Long-endurance flight path.

$$J = \left[\frac{v}{(\omega/2\pi)d}\right] \tag{3}$$

Airspeed v is calculated from the dynamic model of the aircraft. The input to the aircraft dynamic model is the thrust from the propeller. The outputs are aircraft airspeed and altitude. The aircraft model assumes a flat earth coordinate system and coordinated turns. The equations of motion of the aircraft are [23]

$$\dot{h} = v \sin\gamma \tag{4}$$

$$\dot{v} = \frac{T\cos\alpha - D}{m} - g\sin\gamma \tag{5}$$

$$\dot{\gamma} = \frac{T\sin\alpha + L}{m}\cos\phi - \frac{g}{v}\cos\gamma \tag{6}$$

Aircraft lift and drag are defined as

$$L = \tfrac{1}{2}\rho v^2 S_w C_L \tag{7}$$

$$D = \tfrac{1}{2}\rho v^2 S_w C_D + mgC_{\text{rr}} \tag{8}$$

The coefficients of lift C_L and drag C_D vary as a function of angle of attack. The coefficient of rolling resistance C_{rr} is 0.008 while the aircraft is in contact with the ground and zero while the aircraft is in flight.

The states of the model are the propeller speed ω, aircraft altitude h, airspeed v, and climb path angle γ. The angle of attack α and bank angle ϕ are static control parameters that are determined by the aircraft flight controller. The propeller and aircraft simulation are run on the control computer, and the thrust and velocity of the aircraft are updated at 4 Hz.

D. Simulated Flight-Path Definition

The aircraft is programmed to fly a virtual mission that consists of four segments: takeoff, climb, long-endurance orbit, and landing. The simulated flight path emulates the path of a generic long-endurance remote sensing mission. The flight path is shown in Fig. 4.

The takeoff segment begins with the states of the aircraft $h = v = \gamma = \omega = 0$. The aircraft attitude is fixed so that $\alpha = \phi = 0$. As the flight simulation begins, the electric motor accelerates, providing thrust to the simulated aircraft. When the aircraft simulation reaches the cruise velocity of the aircraft in flight, the autopilot controller rotates the aircraft to $\alpha > 0$ and the aircraft simulation takes flight.

During the climb segment, the aircraft attitude is fixed so that $\phi = 0$ deg and $\alpha = 6$ deg. The aircraft controller holds the aircraft velocity constant through elevator deflection, leading to a dynamic $\dot{h}$ of between 30 and 40 m/ min. The aircraft climbs to an altitude of 100 m before transitioning to cruising flight. The long-endurance segment consists of a cruising flight path that circles slowly over a target. The aircraft executes a coordinated turn of radius 1000 m at a constant $\alpha = 7.4$ deg and $v = 13.3$ m/s. The aircraft orbits over its target until the hydrogen tank is nearly empty and then begins the landing segment.

The landing segment is modeled as a spiral gliding descent from the cruise altitude. The aircraft reaches the ground $h = 0$ at approximately the same location where the takeoff began.

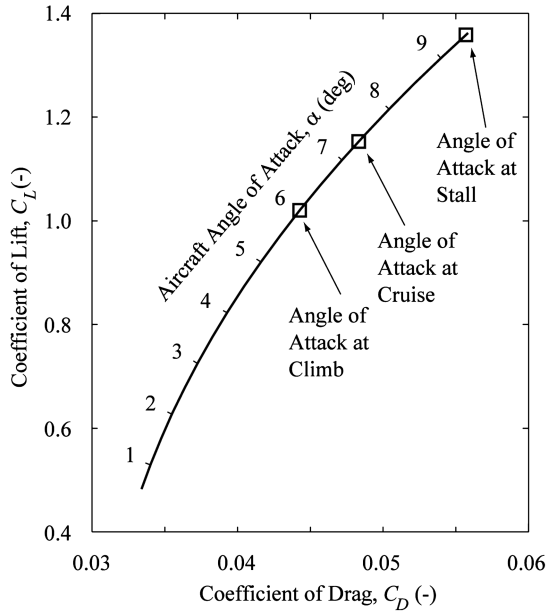

Fig. 5 Aerodynamic characteristics of the airframe under HIL test.

E. Aircraft Description

The aircraft considered in this study is a fuel-cell-powered, propeller-driven UAV. The airframe is a low wing monoplane for which the design and mass are derived from testing of a fuel cell demonstrator aircraft that was successfully flown in 2006 [13]. The aerodynamic characteristics of the HIL aircraft are modeled using a potential flow analysis [20] with experimental corrections and are presented in Fig. 5. The cruise and climb angles of attack are chosen as a compromise between higher airframe efficiency at higher angles of attack and proximity to the estimated stall point at a fuselage angle of attack of $\alpha = 9.5$ deg.

A summary of the aircraft characteristics is presented in Table 1. Compressed hydrogen is stored onboard the aircraft in a composite overwrapped pressure vessel (Carleton Technologies PN6109) at a maximum pressure of 31 MPa. The propeller (Landing Products 20.5×14.5) has a diameter of 52.1 cm and a nominal pitch of 35.6 cm. The aerodynamic performance of the propeller is modeled using an experimentally validated implementation of Goldstein's vortex theory of propellers [24]. The inputs to the propeller software model are shown as a function of advance ratio in Fig. 6.

IV. Experimental Results

This section provides sample results of the HIL simulated long-endurance flight of the fuel-cell-powered UAV described previously.

Table 1 Characteristics of the simulated aircraft

Aircraft characteristic	Value
Gross takeoff mass	12.5 kg
Hydrogen fuel mass	0.206 kg
Powerplant and tank mass	7.40 kg
Cruise lift-to-drag ratio	24.0
Wing area	1.08 m^2

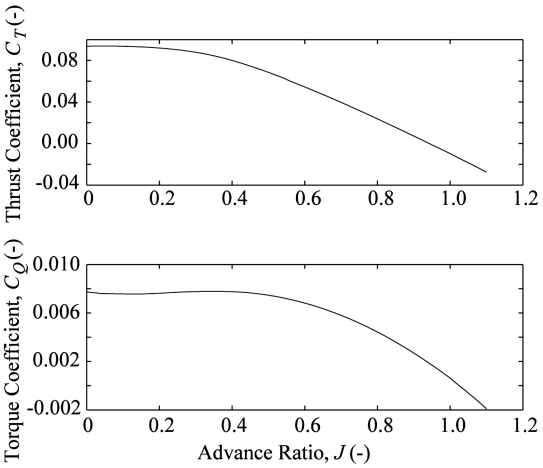

Fig. 6 Propeller performance specifications.

HIL testing was performed in a controlled laboratory environment at a constant 23°C and 37% relative humidity. Cathode flow rate is controlled as a function of stack temperature but is a constant ∼200 liter/ min for a majority of the climb and cruise segments of the HIL test.

A data acquisition system monitors and records the conditions of operation of the test equipment, hardware, and software. The principal measured signals with their associated closed-loop uncertainty at cruise are presented in Table 2. All uncertainties are presented as standard deviations propagated using the methods of [25]. For the purposes of this study, the dynamics of the aircraft and propeller models are treated as deterministic and accurate [20,24].

Figure 7 shows the performance of the aircraft hardware simulation as it completes a subset of the simulated flight. At a time of 0.002 h, the fuel cell current increases and the potential of the fuel cell decreases as the aircraft begins the takeoff segment of the flight test. The simulated aircraft begins to climb after it reaches takeoff speed. The hydrogen consumption of the powerplant increases with increasing fuel cell stack current. The periodic purges of the fuel cell anode manifold are visible as spikes in the hydrogen flow rate. At a time of 0.065 h, the simulated aircraft has reached its cruising altitude of 100 m, and the aircraft enters the cruise segment of the flight test. The potential of the fuel cell increases and the current decreases as the power output of the powerplant decreases to match the cruise power of the aircraft. After the climbing flight segment, the aircraft cruises at steady level flight conditions.

Figure 8 shows the behavior of the aircraft powerplant for the entirety of the long-endurance flight. During the long-endurance cruise, the aircraft flies at steady speed and altitude. After the early potential excursions associated with the takeoff and climbing flight segments, there is a slight decrease in the measured output voltage of the fuel cell stack over the remainder of the test. The fuel cell potential decreases from the short period value of approximately 46 V to a steady-state value of approximately 40 V. This behavior is analyzed more completely in the Sec. V.

The actual duration of the HIL flight simulation is 22.75 h. After this period, the aircraft has consumed all of the hydrogen carried onboard. The experimental endurance of the aircraft for this HIL experiment is 22.75 ± 0.64 h, with experimental uncertainty.

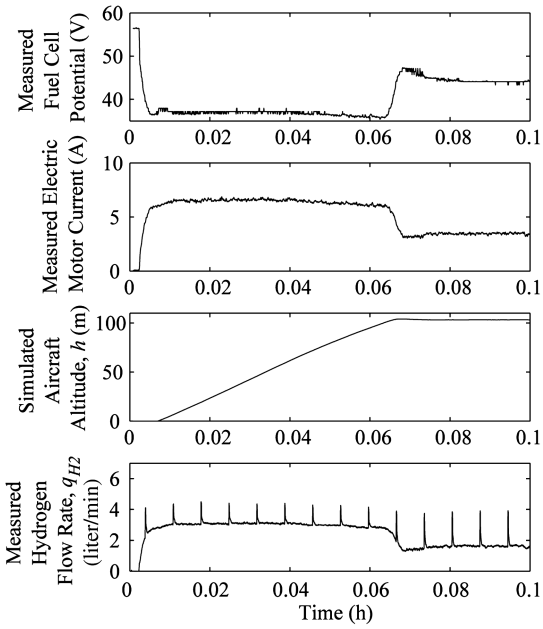

Fig. 7 HIL simulation performance during takeoff and climb flight segments.

V. Discussion

A. Power Train Performance at Cruise

A challenge to the development of fuel cell powerplants for aircraft is characterization of the low-level performance and efficiency of the powerplant components under flight conditions. When available, these data can be used to guide component specification, tuning, and low-level design decisions. UAVs are an especially difficult application for data acquisition because of their small-scale, limited available payload power and mass and poor experimental repeatability due to varying atmospheric and flight conditions. HIL allows this low-level data to be gathered because HIL testing is performed under laboratory-controlled conditions accessible to large-scale, high-rate data acquisition systems. As such, measurements that might be very difficult to make during flight can be made with improved resolution and low experimental uncertainty.

Figure 9 shows a detailed breakdown of the power consumption and output of each major powerplant and power train component. Each powerflow is labeled with its measured or simulated uncertainty over 10,000 samples of the cruise flight segment. These are determined under the same conditions of flight as shown in Table 2.

The power input to the fuel cell stack is a flow of hydrogen gas. The lower heating value of hydrogen is 120.1 MJ/kg, and the flow has an equivalent average power of 307 ± 8 W. Approximately 10% of the flow of hydrogen is released unreacted to the environment from the periodic purging of the anode manifold. The dc electrical output power of the fuel cell is split between the payload and balance of plant and the electric motor. The conversion efficiency of the fuel cell system from hydrogen flow to dc electrical power is 52 ± 8%. The electric motor converts electrical power to rotational power at 71 ± 4%. The propeller simulation finds that the propeller is 69 ± 3% efficient at cruise, producing 70 ± 3 W of propulsive power.

Table 2 Values and uncertainty for the primary data acquired during testing

Measured signal	Nominal value at cruise	Total uncertainty	Percentage uncertainty, %	Sampling period, s
Fuel cell system current	3.56 A	0.207 A	5.82	0.25
Fuel cell system voltage	40.04 V	0.454 V	1.13	0.25
Motor output torque	0.43 N · m	0.005 N · m	1.27	0.25
Motor rotational speed	235.30 rad/s^{-1}	6.320 rad/s^{-1}	2.68	0.25
Hydrogen flow rate	1.54 liter/min^{-1}	0.042 liter/min^{-1} ≡	2.75	0.05

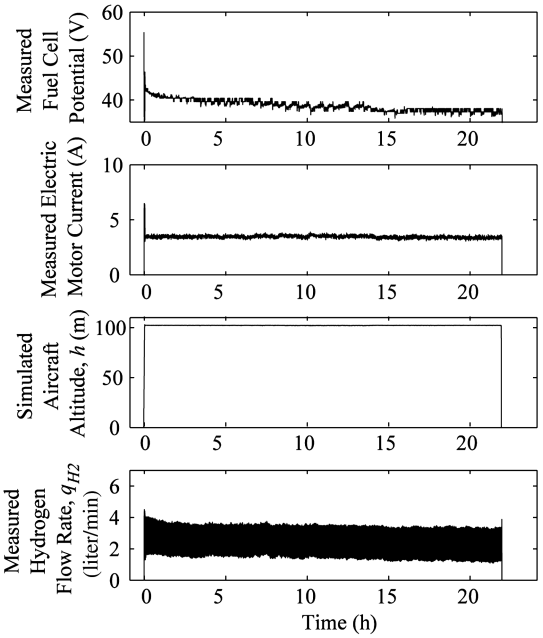

Fig. 8 HIL simulation performance during the entire long-endurance flight.

These results show that the HIL simulation can be used to effectively characterize the powerplant performance inclusive of system interactions and at flight conditions. Concurrent optimization of both software and hardware components during the development of this UAV powerplant allowed for the definition of the optimal configuration used for these tests.

B. Dynamic Powerplant Performance Under Hardware-in-the-Loop Testing

Advanced UAV powerplant systems often exhibit unmodeled dynamics, performance uncertainty, or tunable control systems. In these cases, HIL testing allows for the detailed evaluation of subsystem performance and system interactions under real world operating conditions and in earlier stages of aircraft development. For example, many of the fuel cell powerplant system design studies performed to date rely on a static fuel cell polarization curve to represent the performance of the fuel cell stack [15,16]. A static polarization curve, such as is shown in Fig. 2, contains intrinsic assumptions regarding stoichiometry, membrane water content,

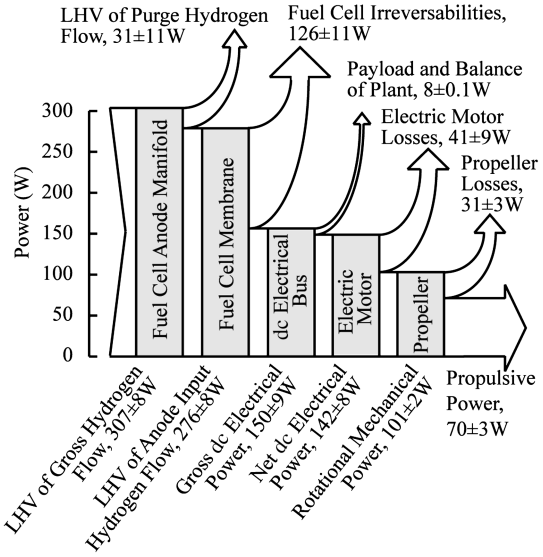

Fig. 9 Propulsion system losses at the cruise condition. (LHV denotes lower heating value.)

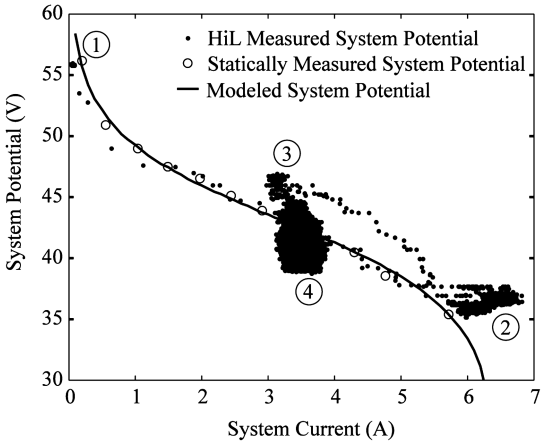

Fig. 10 Horizon H300 fuel cell system polarization curve for a long-endurance HIL test.

ambient conditions, and stack temperature. The dynamic behavior of fuel cell stacks is often different from their static behavior in ways that can influence the effectiveness of a fuel cell system design. This section will discuss the unmodeled dynamics of the fuel cell powerplant during the HIL simulation.

Figure 10 shows the potential and current of the fuel cell system during the long-endurance fuel cell HIL test. At idle, the fuel cell stack operates at low current and 56 V at point 1. As the aircraft accelerates and takes off, the fuel cell operating condition moves along the polarization curve to the high current, low potential condition at point 2. Near point 2, the aircraft is climbing and the fuel cell stack is operating at approximately 6.7 A and 38 V. At this condition, the current and potential of the fuel cell system are higher during the HIL test than during the static experimental test. This suggests that the conditions of use of the fuel cell during the HIL test are causing the fuel cell system to momentarily outperform its steady-state performance. The causes of these dynamics could not be definitively assessed from these experiments, but membrane hydration dynamics often occur at these time scales [26]. It is hypothesized that the low stack temperature, due to the stack not having reached thermal steady state (see Fig. 11), reduces the evaporation rate at the cathode allowing more liquid water to remain in the membrane, thereby reducing the fuel cell overpotential.

After the climb segment, the power required by the aircraft decreases as it enters the cruise segment. The fuel cell system moves to a current of 3.2 A and a potential of 47 V at point 3. For a short period after the high current operation, the potential is higher than the modeled steady-state operating potential of the fuel cell stack. This reduction in overpotential seems to occur because the fuel cell stack is at a higher measured operating temperature (see Fig. 11) and

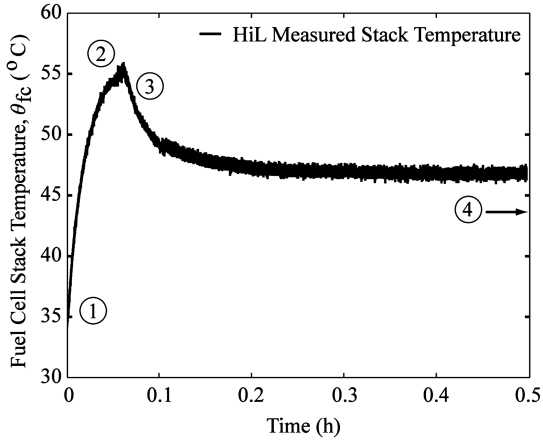

Fig. 11 First portion of a long-endurance HIL test. (Labels correspond to those from Fig. 10.)

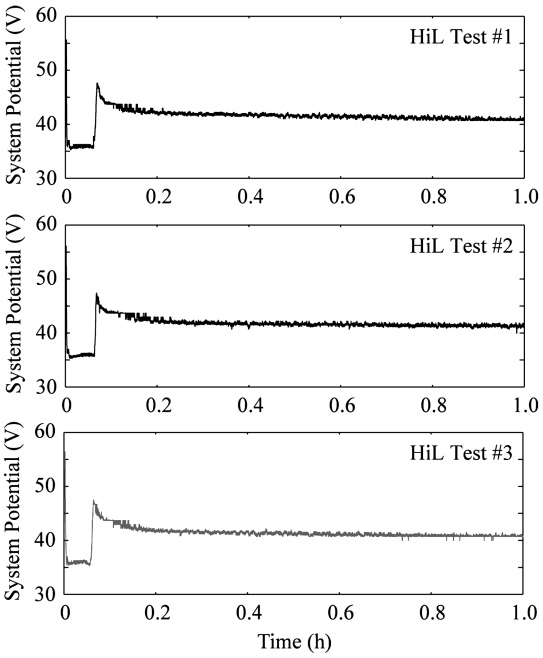

Fig. 12 Comparison of fuel cell stack dynamics among subsequent long-endurance HIL tests showing excellent repeatability.

higher water content than steady state. Over the course of the next few hours, the system settles along a line of constant power into an operating point at lower voltage and higher current at point 4. The increase in overpotential could be due to changes in membrane water content [26], the slow growth of surface oxides on the cathode catalysts during cruise [27], current transients at the electric motor commutation frequency, or other uncontrolled system-level effects, but it was not explored in detail. These voltage dynamics of the fuel cell system under HIL testing are consistent and repeatable, as shown in Fig. 12.

The unmodeled voltage dynamics have a considerable effect on the performance of the aircraft. For instance, the lower than predicted stack potential during cruise lowers the efficiency of the fuel cell powerplant and reduces the endurance of the aircraft system. As shown in Fig. 8, the stack performs components of the long-endurance test at a potential as low as 39 V instead of its predicted potential of 42.3 V. In the hydrogen/air fuel cell system, the efficiency of the fuel cell stack can be approximated as

$$\eta_{\text{stack}} = \frac{V}{n_{\text{cells}} E^{\text{O}}} \in \tag{9}$$

Using (9), the efficiency of the fuel cell stack as predicted from the static polarization curve is 54%. Under HIL testing, the efficiency of the stack is as low as 51%, thereby reducing the endurance of the aircraft by approximately 5.6% relative to its static design point.

By quantifying the unmodeled performance of the fuel cell stack, HIL simulation allows the aircraft designer to assess the real world performance of the aircraft system. In addition, the effects of system interactions, unmodeled operating conditions, environmental variables, and component degradation can all be assessed consistently without constructing and testing entire aircraft systems.

C. UAV Powerplant Performance Comparison

The literature contains only a few examples of fully developed fuel cell powerplants for aircraft [3,16,28]. To date, comparisons of the theoretical performance of electrochemical and internal combustion powerplants in the UAV application have used idealized, non-validated data sets [3,19]. The results of this study now provide a designed, constructed and tested proton exchange membrane (PEM) fuel cell powerplant for which the performance can be used to compare the as-realized performance of UAV powerplant technologies, using similar results from the literature. This section of the discussion will present a first-order analytical comparison between the performance of aircraft incorporating various energy storage technologies.

Using Newton's laws, a simplified range equation for the aircraft can be derived in which the weight is constant (as is appropriate for the UAVs with electrochemical energy storage):

$$ds = \int \frac{\mathrm{d}E}{T} \tag{10}$$

For steady level flight $T = D$ and $L = mg$,

$$s = \left(\frac{E}{D}\right) = \left(\frac{L}{D}\right)\left(\frac{E}{L}\right) = \left(\frac{E}{m}\right)\left(\frac{C_L}{gC_D}\right) \tag{11}$$

A similar approach can be followed to derive a simplified endurance equation for an aircraft at steady level flight:

$$T = \frac{C_D}{C_L} W \tag{12}$$

Rearranging Eq. (7) with $W = L$,

$$v = \left[\frac{W}{\frac{1}{2}(\rho S_w C_L)}\right]^{1/2} \tag{13}$$

The propulsive output energy is the integral of the propulsive output power:

$$E = \int_0^t \frac{C_D}{C_L} W \left[\frac{W}{\frac{1}{2}(\rho S_w C_L)}\right]^{1/2} \mathrm{d}t \tag{14}$$

Under the assumption that the weight of the aircraft changes negligibly over the course of the flight,

$$E = \frac{C_D t}{\sqrt{\frac{1}{2}(\rho S_w)}} \left(\frac{W}{C_L}\right)^{3/2} \tag{15}$$

Solving for the aircraft endurance,

$$t = \left(\frac{E}{m^{3/2}}\right)\left(\frac{(\frac{1}{2}\rho S_w)^{1/2} C_L^{3/2}}{g^{3/2} C_D}\right) \tag{16}$$

To compare the range and endurance performance of the fuel-cell-powered aircraft to other electrochemical energy storage technologies, we can evaluate the quantities E/m and $E/m^{3/2}$.

To construct a comparison to the variable mass internal combustion powerplant, we can numerically integrate (14) under the assumptions of constant airspeed v, varying mass $m = W/g$ due to fuel consumption at constant I_{sp}, a controllable angle of attack α, and the aircraft aerodynamic characteristics shown in Fig. 5. The result is a nonlinear system of summation equations discretized in time that can be solved for the endurance and range of the internal combustion UAV.

These comparisons assume that the airframe mass is the same for each technology. Electric motor mass (283 g), fuel mass, and fuel tank mass (5% of the fuel mass for hydrocarbon fuels) are included where appropriate. For all powerplants, propeller efficiency is a constant 69% and for all electric powerplants, motor efficiency is a constant 71%. For the internal combustion engine, the payload and aircraft control power is produced assuming an alternator of 80% efficiency. The specifications of the energy storage subsystems come from the literature or the results of the fuel cell UAV HIL tests. The endurance and range of the aircraft designs are limited by the requirement that each powerplant is sized to have the same takeoff weight as the HIL aircraft. By designing an aircraft using these assumptions, these energy storage subsystem performance metrics can be translated into aircraft-level performance metrics E/m and $E/m^{3/2}$. Equations (11) and (16) can then be used to calculate the range and endurance of the designed aircraft.

Table 3 Comparison of electrochemical powerplants for long-range and long-endurance missions in small-scale aircraft

Powerplant type	Energy storage subsystem specifications	(E/m)	$(E/m^{3/2})$	Calculated range s, using Eq. (11)	Calculated endurance t, using Eq. (16)
HIL hydrogen PEM fuel cell	448 dcW · h/kg	124.9 W · h/kg	35.3 W · h/(kg)$^{3/2}$	1100 km	24.1 h
Zinc–air battery	350 dcW · h/kg [5]	101.4 W · h/kg	28.7 W · h/(kg)$^{3/2}$	894 km	19.6 h
Lithium–polymer battery	166 dcW · h/kg [a]	48.1 W · h/kg	13.6 W · h/(kg)$^{3/2}$	423 km	9.3 h
Small internal combustion engine	0.3 kg of fuel/h^{-1} at 105 W[19]	124.7 W · h/kg	124.7 W · h/(kg)$^{3/2}$	1083 km	23.8 h

[a]Sanyo Electric Company, lithium–polymer rechargeable batteries product literature, 10 Oct. 2002.

The first result of these comparisons among energy storage technologies is shown in the first three rows of Table 3. For each technology, Table 3 presents a characterization of the energy storage subsystems at this scale, the performance metrics E/m and $E/m^{3/2}$, and the range and endurance calculated using Eqs. (11) and (16). Comparing the characteristics of the energy storage subsystems among the first three rows of Table 3 shows that the specific energy of the HIL PEM fuel cell energy storage system is significantly higher than the specific energy of both zinc–air batteries and lithium–polymer batteries. This translates into higher aircraft performance metrics and higher aircraft endurance and range for the PEM fuel-cell-powered UAV. In other words, using commercially available compressed hydrogen storage and fuel cell systems, a small-scale hydrogen fueled PEM UAV can enable longer range and endurance than other electrochemical energy storage systems, including zinc–air and lithium–polymer batteries. For long-endurance or long-range applications, for which electrically powered UAVs are preferred, the fuel cell powerplant offers the highest performance. The endurance of the HIL hydrogen PEM fuel cell aircraft in Table 3 is slightly higher than the HIL tested endurance because (16) does not include the energy consumed during takeoff.

The second result of this analysis is a comparison of the performance of the fuel cell aircraft, shown in the first row of Table 3, to the performance of the internal combustion engine aircraft, shown in the final row of Table 3. The comparison shows that the specific energies, endurance, and range of the internal combustion aircraft are approximately equal to those of the PEM fuel cell aircraft. This result suggests that the scale of the HIL aircraft is near the crossover point for comparing these technologies in the long-endurance and long-range UAV application. Although further development will improve the performance of both the PEM fuel cell powerplant and the internal combustion engine, this analysis provides a basis for validated comparison of powerplant hardware at the scale of the designed and tested fuel cell UAV.

VI. Conclusions

This paper proposes a HIL simulation architecture for system-level performance, range, and endurance testing of a fuel cell UAV powerplant. For this study, the UAV powerplant hardware is embedded within the main aircraft dynamics loop and the energy storage hardware is coupled to the simulation by a dc electrical bus. The interface between the software simulation of the aircraft dynamics and the powerplant hardware is provided by a torque- and speed-controlled dynamometer and signal conditioning hardware. Testing of the performance and endurance of a PEM fuel-cell-powered UAV is performed by simulating the flight of the aircraft over a generic long-endurance remote sensing mission. The aircraft exhibits a measured climb rate of up to 40 m/min^{-1} and a flight endurance of 22.75 ± 0.64 h, providing validation of the viability and performance of this fuel-cell-powered aircraft.

Measurements of the powerflows within the aircraft powerplant quantify the efficiencies and losses of each major powerplant component. The dynamic performance of a fuel cell system under real world conditions is assessed and compared to static models. This analysis shows that the unmodeled dynamics of the fuel cell powerplant can have a significant effect on the efficiency and endurance of the aircraft. The performance of the PEM fuel cell powerplant used in this study is then contrasted with state-of-the-art electrochemical energy storage technologies and internal combustion engines. The fuel cell powerplant constructed for this study can outperform other available electrochemical energy storage technologies in key metrics for long-endurance or long-range missions. Its performance in these key metrics is comparable to the performance of an internal combustion engine powerplant at similar scale.

Acknowledgments

This work was funded in part by the NASA University Research, Engineering, and Technology Institute at the Georgia Institute of Technology. The authors would like to thank the research engineers at the Georgia Tech Research Institute's Aerospace, Transportation, and Advanced Systems Laboratory and Aerospace Systems Design Laboratory for their assistance. The authors would also like to thank Mohammad Kapacee and Orion King of the Woodruff School of Mechanical Engineering for their contributions.

References

[1] Reid, C. M., Manzo, M. A., and Logan, M. J., "Performance Characterization of a Lithium-Ion Gel Polymer Battery Power Supply System for an Unmanned Aerial Vehicle," NASA TM2004-213401, 2004.

[2] Curtis, J. B., Charette, J. G., Spear, D. F., Bode, J. V., III, and Brandt, S. A., "Aerodynamic Optimization of the Lockheed-Martin FPASS/Desert Hawk UAV," AIAA Paper 2004-6607, Sept. 2004.

[3] Bradley, T. H., Moffitt, B., Parekh, D., and Mavris, D., "Development and Experimental Characterization of a Fuel Cell Powered Aircraft," *Journal of Power Sources*, Vol. 171, No. 2, 2007, pp. 793–801. doi:10.1016/j.jpowsour.2007.06.215

[4] Agarwal, G., "Lithium Peroxide Fuel Cells for Electric Vehicle Propulsion," *Journal of Propulsion and Power*, Vol. 16, No. 2, 2000, pp. 367–369. doi:10.2514/2.5579

[5] Putt, R., Naimer, N., and Atwater, T., "Fourth Generation Zinc–Air Batteries," *Proceedings of the 41st Power Sources Conference*, June 2004.

[6] Fleming, J., Ng, W., and Ghamaty, S., "Thermoelectric-Based Power System for Unmanned-Air Vehicle/Micro Air Vehicle Applications," *Journal of Aircraft*, Vol. 41, No. 3, 2004, pp. 674–676. doi:10.2514/1.11486

[7] Harmon, F. G., Chattot, J. J., and Frank, A. A., "Conceptual Design and Simulation of a Small Hybrid-Electric Unmanned Aerial Vehicle," *Journal of Aircraft*, Vol. 43, No. 5, 2006, pp. 1490–1498. doi:10.2514/1.15816

[8] Fathy, H. K., Filipi, Z. S., Hagena, J., and Stein, J. L., "Review of Hardware-in-the-Loop Simulation and Its Prospects in the Automotive Area," *Proceedings of SPIE*, Vol. 6228, 2006, pp. 1–20. doi:10.1117/12.667794

[9] Mackall, D. A., "Qualification Needs for Advanced Integrated Aircraft," NASA TM-86731, Aug. 1985.

[10] Kosmatka, J. B., "Development of a Long-Range Small UAV for Atmospheric Monitoring." AIAA Paper 2007-2234, April 2007.

[11] Bateman, T. A., Nelson, J. D., and Argrow, B. M., "A Low-Cost Rapid Construction Unmanned Aircraft Design," AIAA Paper 2007-2703, May 2007.

[12] Tigner, B., Meyer, M. J., Holden, M. E., Rawdon, B. K., Page, M. A., Watson, W., and Kroo, I., "Test Techniques for Small Scale Research Aircraft," AIAA Paper 98-2726, June 1998.

[13] Bradley, T. H., Moffitt, B., Thomas, R. W., Mavris, D., and Parekh, D. E., "Test Results for a Fuel Cell-Powered Demonstration Aircraft," Proceedings of the Society of Automotive Engineers Power System Conference, Society of Automotive Engineers Paper 2006-01-3092,

Nov. 2006.
[14] Howard, R. M., Tanner, J. C., and Lyons, D. F., "Flight Test of a Half-Scale Unmanned Air Vehicle," *Journal of Aircraft*, Vol. 28, No. 12, 1991, pp. 843–848. doi:10.2514/3.46107
[15] Moffitt, B., Bradley, T. H., Mavris, D., and Parekh, D. E., "Reducing Design Uncertainty of a Fuel Cell UAV Through Variable Fidelity Optimization," AIAA Paper 2007-7793, Sept. 2007.
[16] Herwerth, C., Chiang, C., Ko, A., Matsuyama, S., Choi, S. B., Mirmirani, M., Gamble, D., Arena, A., Koschany, A., Gu, G., and Wankewycz, T., "Development of a Small Long Endurance Hybrid PEM Fuel Cell Powered UAV," Society of Automotive Engineers Paper 2007-01-3930, Sept. 2007.
[17] PHILipps, S. P., and Ziegler, C., "Computationally Efficient Modeling of the Dynamic Behavior of a Portable PEM Fuel Cell Stack," *Journal of Power Sources*, Vol. 180, No. 1, 2008, pp. 309–321. doi:10.1016/j.jpowsour.2008.01.089
[18] Xu, H., Kunz, H. R., and Fenton, J. M., "Investigation of Platinum Oxidation in PEM Fuel Cells at Various Relative Humidities," *Electrochemical and Solid-State Letters*, Vol. 10, No. 1, 2007, pp. B1–B5. doi:10.1149/1.2372230
[19] Menon, S., Moulton, N., and Cadou, C., "Development of a Dynamometer for Measuring Small Internal-Combustion Engine Performance," *Journal of Propulsion and Power*, Vol. 23, No. 1, 2007, pp. 194–202. doi:10.2514/1.19825
[20] PHILlips, W. F., and Snyder, D. O., "Modern Adaptation of Prandtl's Classic Lifting-Line Theory," *Journal of Aircraft*, Vol. 37, No. 4, 2000, pp. 662–670. doi:10.2514/2.2649
[21] Kulikovsky, A. A., "The Effect of Stoichiometric Ratio on the Performance of a Polymer Electrolyte Fuel Cell," *Electrochimica Acta*, Vol. 49, No. 4, 2004, pp. 617–625. doi:10.1016/j.electacta.2003.09.016
[22] PHILlips, W. F., *Mechanics of Flight*, Wiley, Hoboken, NJ, 2004.
[23] Chen, R. H., and Speyer, J. L., "Improved Endurance of Optimal Periodic Flight," *Journal of Guidance, Control, and Dynamics*, Vol. 30, No. 4, 2007, pp. 1123–1133. doi:10.2514/1.27313
[24] Moffitt, B., Bradley, T. H., Mavris, D., and Parekh, D. E., "Vortex Propeller Model Generation and Validation with Uncertainty Analysis for UAV Design," AIAA Paper 2008-406, Jan. 2008.
[25] Kline, S. J., and McClintock, F. A., "Describing Uncertainties in Single-Sample Experiments," *Mechanical Engineering*, Vol. 75, 1953, pp. 3–7.
[26] Hamelin, J., Agbossou, K., Laperriere, A., Laurencelle, F., and Bose, T. K., "Dynamic Behavior of a PEM Fuel Cell Stack for Stationary Applications," *International Journal of Hydrogen Energy*, Vol. 26, No. 6, 2001, pp. 625–629. doi:10.1016/S0360-3199(00)00121-X
[27] Donahue, J., Fuller, T. F., Yang, D., and Yi, J. S., UTC Fuel Cells, South Windsor, CT, U.S. Patent No. 6,399,231 for "Method and Apparatus for Regenerating the Performance of a PEM Fuel Cell," issued 04 June 2002.
[28] Stroman, R. O., and Kahn, A., "Development and Integration of Controls for a PEMFC Powered Aircraft," *Electrochemical Society Transactions*, Vol. 11, No. 1, 2007, pp. 1493–1504 .

C. Tan
Associate Editor